

pubs.acs.org/JPCC Article

Sn-Induced Synthesis of Highly Crystalline and Size-Confined Si Nanorods at Moderately High Temperatures Using Hydrogen Silsesquioxane

Griffin C. Spence, Rachel C. Barbieri, David Pate, Lisa S. Graves, Ümit Özgür, and Indika U. Arachchige*



Cite This: J. Phys. Chem. C 2023, 127, 11579–11590



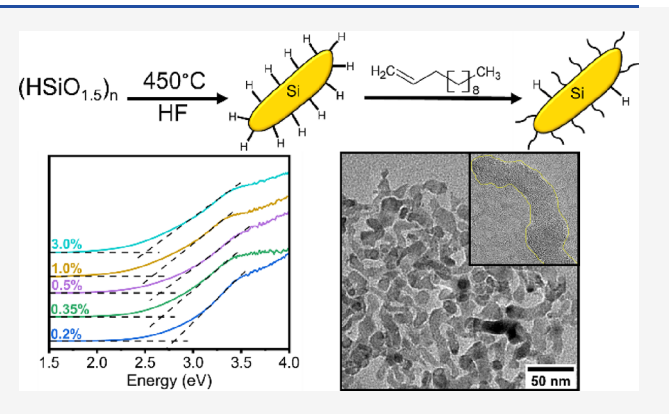
ACCESS I

Metrics & More

Article Recommendations

s Supporting Information

ABSTRACT: Size-confined Si nanorods (NRs) have gained notable interest because of their tunable photophysical properties that make them attractive for optoelectronic, charge storage, and sensor technologies. However, established routes for fabrication of Si NRs use well-defined substrates and/or nanoscopic seeds as promoters that cannot be easily removed, hindering the investigation of their true potential and physical properties. Herein, we report a facile, onestep route for the fabrication of Si NRs via thermal disproportionation of hydrogen silsesquioxane (HSQ) in the presence of a molecular tin precursor (SnCl₄) at a substantially lower temperature (450 °C) compared to those used in the synthesis of size-confined Si nanocrystals (>1000 °C). The use of these precursors allows the facile isolation of phase-pure Si NRs via HF etching and subsequent surface passivation with 1-dodecene via hydrosilylation. The



diameters (7.7–16.5 nm) of the NRs can be controlled by varying the amount of SnCl₄ (0.2–3.0%) introduced during the HSQ synthesis. Physical characterization of the NRs suggests that the diamond cubic structure is not affected by SnCl₄, HF etching, and hydrosilylation. Surface analysis of NRs indicates the presence of Si⁰ and Siⁿ⁺ species, which can be attributed to core Si and surface Si species bonded to dodecane ligands, respectively, and a systematic variation of the Si⁰:Si–C ratio with the NR diameter. The NRs show strong size confinement effects with solid-state absorption onsets (2.51–2.80 eV) and solution-state (Tauc) indirect energy gaps (2.54–2.70 eV) that can be tuned by varying the diameter (16.5–7.7 nm). Photoluminescence (PL) and time-resolved PL (TRPL) studies reveal size-dependent emission (1.95–2.20 eV) with short, nanosecond lifetimes across the visible spectrum, which trend closely with absorption trends seen in solid-state absorption data. The facile synthesis developed for size-confined Si NRs with high crystallinity and tunable optical properties will promote their application in optoelectronic, charge storage, and sensing studies.

INTRODUCTION

Semiconducting nanomaterials are promising materials for the future of electronic and optoelectronic devices such as solar cells, $^{1-3}$ bioimaging, 4,5 lithium-ion batteries, $^{6-8}$ transistors, 9,10 and optoelectronic devices. 11,12 The majority of direct-gap semiconducting nanomaterials, such as Cd and Pb chalcogenide QDs, are popular because of their efficient light-harvesting properties and size- and shape-dependent optical properties that arise from quantum confinement effects, but these nanomaterials are less desirable for biological or environmental applications due to their high toxicity. 13-16 As a result, interest has shifted toward Group IV semiconducting nanomaterials, Si and Ge, which are inherently less toxic and more compatible with the current industry standard of Si for integrated circuits. 15,17 Yet, one downside with Group IV materials is that these materials exhibit an indirect band gap, which will drastically impact their ability to absorb and emit light. 15,18,19 Fortunately, size confinement can be employed to improve

light—matter interactions and cause an indirect- to direct-gap transition in nanomaterials like Si and Ge. ^{20,21} Silicon has also found promise in electronic niches such as lithium-ion batteries due to its high theoretical specific capacity (4200 mA h g⁻¹), much higher than that of commercial graphite (370 mA h g⁻¹). ^{17,22}

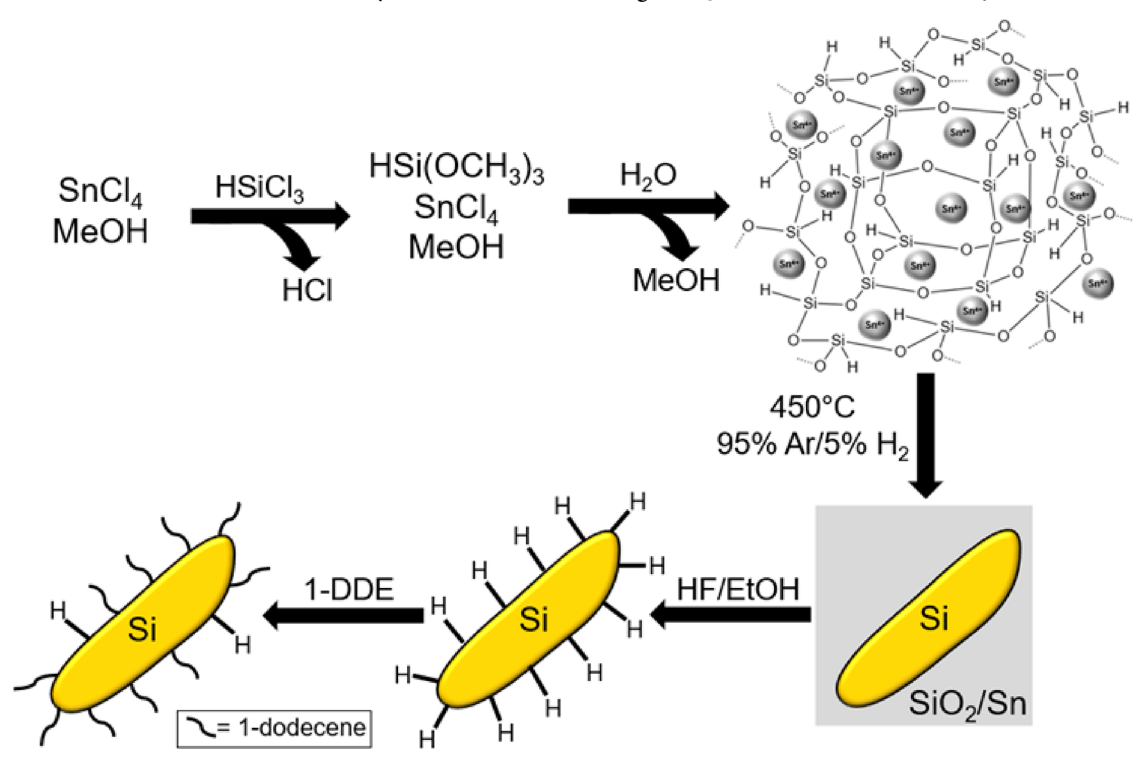
Of the popular Group IV semiconducting materials, Si has emerged as the principal material for device applications due to its high abundance, low toxicity, and compatibility with complementary metal—oxide—semiconductor (CMOS) standards.^{20,23} Although bulk Si has an indirect band gap, at the

Received: February 25, 2023 Revised: May 25, 2023 Published: June 12, 2023





Scheme 1. A Schematic Illustration of the Synthesis of Si NRs Using HSQ in the Presence of SnCl₄^a



"SnCl₄ and HSQ were simultaneously thermally disproportionated and reduced, respectively, to produce Si NRs embedded in a matrix of SiO₂ and β -Sn crystals. Phase-pure Si NRs were isolated via HF etching followed by passivation with 1-dodecene (1-DDE) via hydrosilylation.

nanoscale, Si NRs show enhanced optical properties such as photoluminescence with UV irradiation for NR diameters less than 5 nm due to strong size confinement effects. As the nanorod diameter increases, however, the luminescence redshifts, and for NR diameters exceeding 5 nm, luminescence was observed in the near-IR spectrum. Because of tunable optical and electronic properties, Si NRs hold promise for a wide range of applications including but not limited to solar cells, charge storage, biosensors, and gas-phase sensors. 6,26-31

Over the past 30 years, there has been a plethora of methods employed to manufacture Si NRs including laser ablation, evaporation of silicon monoxide, molecular beam epitaxy, metal-assisted chemical etching, laser-induced etching, and many more. 32-37 However, the majority of these methods have similar drawbacks including low size tunability, extreme reaction conditions, and/or the necessity of metal seeds (Au, Ag, Sn, Al, and Ni), usually in the form nanocrystals, as promoters for NR growth ^{24,35,38-42} (Table S1). Additionally, the majority of the nanowires/nanorods produced have diameters too large to exhibit any confinement affects. To circumvent these challenges, Sn can be added as a promoter for Si NR growth and crystallization. Similar to many metal seeds, Sn can quench the optical properties but can be easily dissolved in common strong acids (HCl and/or HF) without affecting the properties of the NR, which allows for facile isolation of phase-pure Si NRs. The influence of Sn on the growth and crystallization of Si NRs at high temperatures has been reported in the literature, studying Sn in the form of a nanocrystal, as a promoter to produce Si NRs.²⁴ Unfortunately, this requires extra complexity, time, and steps to synthesize the nanocrystals before producing any NRs.

Herein, we report the synthesis of silicon NRs using a modified route via thermal disproportionation of HSQ in the

presence of a simple molecular Sn promoter, SnCl₄ (Scheme 1). SnCl₄ can be homogeneously distributed in the HSQ matrix during HSQ synthesis. The sensitivity of the concentration of SnCl₄, 0.2-3.0%, in the system allows for control over the NR length and diameter from 50 to 120 nm and 7.7 to 16.5 nm, respectively. The structural and surface characteristics of the NRs were probed using powder X-ray diffraction (PXRD), transmission electron microscopy (TEM), Raman, Fourier transform infrared (FTIR), and X-ray photoelectron spectroscopy (XPS). It was found that both SiO2 and Sn can be efficiently removed through HF etching to produce H-terminated Si NRs without altering the morphology and preserving the high crystallinity. XPS and FTIR were used to investigate the effects of surface passivation by dodecane ligands and the variation in the ratio of core silicon (Si-Si) bonds to surface silicon-to-ligand (Si-C) bonds, which showed an increase with an increasing NR diameter. The efficient surface passivation of Si NRs by dodecane ligands has also been qualitatively seen by improved colloidal stability in nonpolar solvents. The effects of size confinement on energy gaps were studied using solid-state diffuse reflectance, solutionstate absorption, and PL/TRPL spectroscopy. As the NR diameter increased, a redshift in solid-state absorption energy onsets (2.80 to 2.51 eV for 0.2-3.0% SnCl₄) was noted, which are slightly larger than solution-state absorption energy gaps (2.70 to 2.48 eV for 0.2-3.0% SnCl₄) obtained from indirectgap Tauc analysis. 43 The solid-state energy gaps trend closely with emission maxima obtained from solid-state PL spectroscopy and those reported in the literature for Si NRs having similar diameters, suggesting strong size confinement effects in as-synthesized Si NRs.^{26,27}

EXPERIMENTAL SECTION

Materials. Trichlorosilane (99%) and tin(IV) chloride (SnCl₄) (99%) were purchased from Sigma Aldrich. 1-Dodecene (96%) was purchased from Alfa Aesar. Hydrofluoric acid (48 to 51%, in water) (HF) was purchased through Fisher or Acros. Common solvents such as methanol (99+ %, MeOH), ethanol (anhydrous and 95%, EtOH), and toluene (99.5%) were ACS grade and purchased from Fisher or Acros. 1-Dodecene was degassed at 115 °C under vacuum for 4 h and stored under a N_2 atmosphere. Methanol was stored under molecular sieves and distilled prior to use. Toluene was dried with sodium and distilled prior to use.

Synthesis of the Hydrogen Silsesquioxane Precursor. The HSQ used in the synthesis of the Si NRs was produced based on a modified method previously reported in the literature. 21 Under N2 atmosphere, 80 mL of MeOH and the appropriate amount of SnCl₄ (Supporting Information, Table S2) were added to a three-neck flask under stirring. Additionally, a syringe was loaded with 4.5 mL of HSiCl₃ and was capped in a sealed vial under N₂. The MeOH/SnCl₄ system was removed from the glovebox, placed in an ice water bath, connected to a Schlenk line, and was continuously flushed with nitrogen. Under rapid stirring, the temperature of the system was cooled to 0-5 °C before HSiCl₃ was injected dropwise via a syringe into the flask, ensuring that the temperature never exceeded 10 °C. After the addition of HSiCl₃, the solution was stirred for 5 min before 18 mL of distilled H₂O was quickly injected, which rapidly increased the temperature to \sim 30 °C. This solution was then stirred for two hours. After two hours, the formed gel was rinsed five times with methanol using a vacuum filtration setup, dried for 5 h at 80 °C on a hot plate, and then stored under vacuum overnight to remove any residual water and MeOH (Scheme 1).

Synthesis of Si NRs Embedded in a Silica Matrix. Si NRs embedded in a silica matrix were synthesized through thermal disproportionation. 18,19,31 HSQ (700 mg) was placed in a ceramic boat and inserted into a tube furnace and was heated to 450 °C for 1 h with a ramp rate of 7 °C/min and under a reducing gas mixture of Ar/H₂ (95%/5%) with a flow rate 20 mL/min. This caused the white solid to change to a brown-black color (Scheme 1).

Liberation of Si NRs from the Silica Matrix. Etching was performed using aqueous HF to liberate phase-pure Si NRs. Caution: Solutions of HF are extremely hazardous and must be used in accordance to local regulations! Neutralization of HF containing waste or spills was performed with a solution of CaCl₂. First, the Si NRs embedded in silica were ground into a powder using a mortar and pestle and added to a polypropylene centrifuge tube. In a N2 atmosphere, 6 mL of EtOH was added to the annealed HSQ and was shaken to achieve a temporary suspension. This was followed by 20 mL of HF, and the solution was stirred for 1 h. To isolate the hydride-terminated NRs, the tube was centrifuged at 6000 rpm for 5 min where the NRs formed a pellet at the bottom of the tube. The clear, colorless supernatant was removed, and 10 mL of fresh, anhydrous EtOH was added to resuspend the NRs. The suspension was centrifuged again at 6000 rpm for 15 min, after which the supernatant was removed. This process was repeated a second time to remove any residual HF leaving a precipitate of hydride-capped Si NRs.

Surface Functionalization via Hydrosilylation. To further improve colloidal stability and protect the surface

from oxidation, thermal hydrosilylation was performed, replacing the hydride capping with a long-chain hydrocarbon. In an inert atmosphere, hydride-terminated Si NRs were dispersed in a three-neck flask containing 20 mL of 1-dodecene. The solution was attached to a Schlenk line and placed under a vacuum and heated at 110 °C for 15 min; then, a nitrogen flow was introduced, and the temperature was increased to 190 °C. This solution was refluxed overnight, allowing optimal surface passivation.

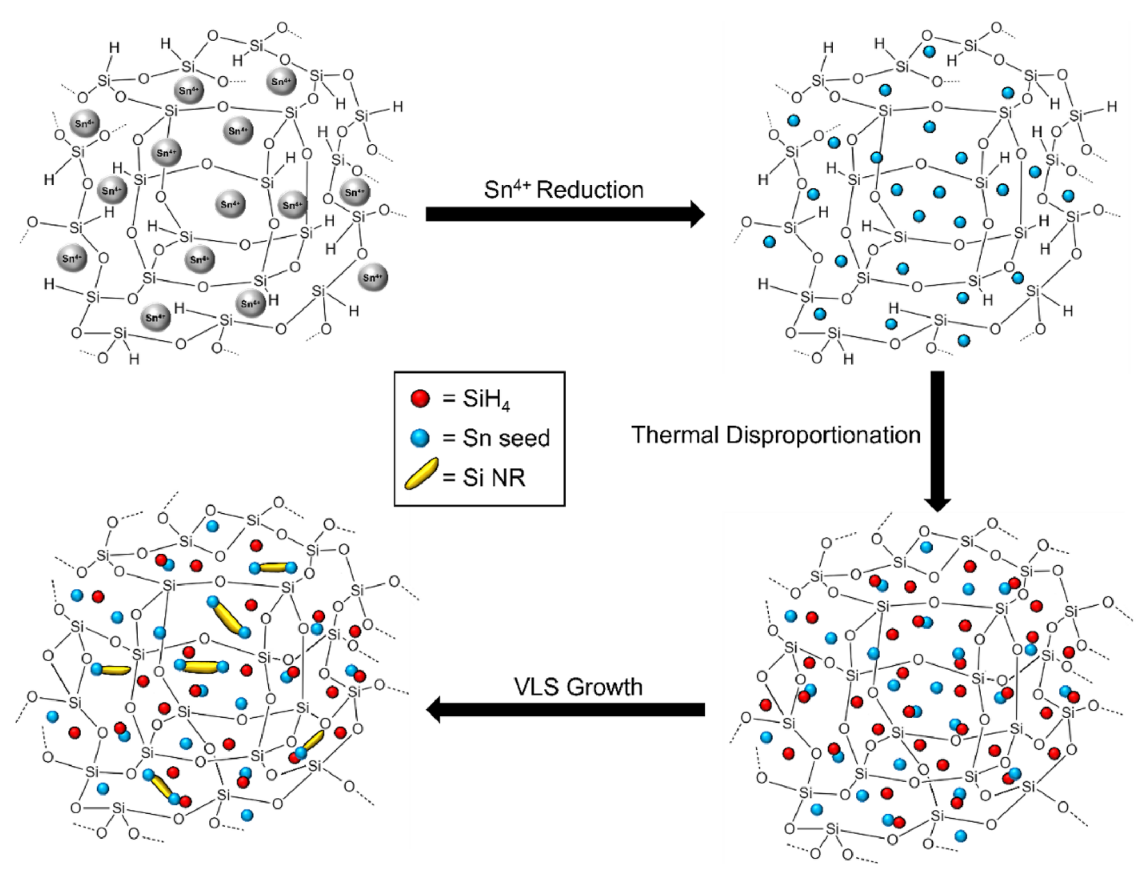
Isolation and Purification. After the hydrosilylation, the NRs were isolated by adding a 3:1 volumetric ratio of MeOH:EtOH to the crude suspension followed by centrifugation at 6000 rpm for 30 min. The supernatant was removed, and 5 mL of toluene was added to the precipitate to redisperse Si NRs. Then, 5 mL of MeOH was added to the Si NRs and centrifuged for 10 min to reprecipitate Si NRs. This procedure was repeated three times to purify Si NRs.

Physical Characterization of Si NRs. Powder diffraction patterns were recorded using a PANalytical powder X-ray diffractometer equipped with a Cu K α (λ = 1.5418 Å) anode. The Scherrer formula was used to calculate the average crystallite size of the NRs. 44 Raman spectra were recorded using a Thermo Scientific DXR Raman spectrophotometer equipped with a 532 nm laser. Low-resolution TEM images were recorded using a Zeiss model Libra 120 electron microscope operating at 120 kV. High-resolution TEM (HRTEM) images and selected-area electron diffraction patterns (SAED) were recorded using a JEOL JEM-F200 cold FEG electron microscope operating at 200 kV. TEM grids were prepared by drop-casting a dilute solution of NRs in toluene onto a lacey carbon-coated copper grid. EDX spectra were recorded using a Hitachi model FE-SEM Su-70 scanning electron microscope (SEM) operating at 15 keV with an in situ EDAX detector. Samples were prepared for SEM by transferring a small amount of NRs onto a carbon tape and then sticking the carbon tape onto an aluminum holder. FTIR spectra were recorded using a Thermo iS50 FTIR. A Thermo Fisher model ESCALAB 250 XPS instrument with an Al K α source was used to record XPS spectra of Si NRs. Solutionstate UV-vis-NIR absorption spectra of the NRs were recorded using a Cary 600i UV-vis-NIR spectrophotometer in the double beam mode. Solid-state diffuse reflectance spectra were recorded using an internal diffuse reflectance DRA 2500 attachment and a BaSO₄ background holder. The Kubelka-Munk remission function was used to convert measured reflectance to absorption data. 45,46 Room-temperature PL spectra of the NRs drop-cast onto Si substrates were measured utilizing a 325 nm HeCd laser in conjunction with a liquid nitrogen-cooled CCD detector mounted onto a 30 cm focal length spectrograph. For TRPL studies, these samples were excited by a Ti:sapphire laser frequency tripled to 266 nm (80 MHz repetition rate, ~70 fs fundamental pulse width), with emission recorded by a Hamamatsu streak camera with an \sim 50 ps resolution.

■ RESULTS AND DISCUSSION

Synthesis and Thermal Disproportionation of HSQ with SnCl₄. Due to the high cost of commercially bought HSQ, lab-made HSQ produced using low-cost precursors was used in the synthesis of Si NRs. ^{18,32} The low-cost HSQ was produced through the hydrolysis and condensation of the HSiCl₃ precursor. Sn was incorporated into HSQ during the synthesis by adding variable amounts of SnCl₄ to MeOH

Scheme 2. Proposed Mechanism for the Thermal Disproportionation of HSQ and Subsequent Synthesis of Si NRs Catalyzed by Sn



followed by HSiCl₃. SnCl₄ reacts with MeOH to form the Sn⁴⁺ precursor and HCl, apparent by a white smoke, which immediately dissolved into solution. HCl produced from both SnCl₄ and HSiCl₃ can also dissolve into and acidify the solution, prevent Si–H bond cleavage of HSi(OCH₃)₃, and catalyze the hydrolysis and condensation reaction. Upon addition of water, acid-catalyzed hydrolysis and condensation of HSi(OCH₃)₃ occurred to produce HSQ.

Once synthesized, the SnCl₄-impregnated HSQ was used to produce Si NRs via thermal disproportionation. This phenomenon has been investigated in the literature but never in the presence of a Sn promoter. 21,49,50 During annealing, HSQ disproportionates at temperatures between 250 and 450 °C to form SiO₂ and SiH₄. This is performed under 95%/5% Ar/H₂ gas to inhibit dehydrogenation side reactions of HSQ that can produce silicon-oxide impurities.⁵¹ Simultaneously, the Sn⁴⁺ precursor can be chemically reduced by H₂ to elemental Sn under elevated temperatures (Scheme 2). We expect this mechanism to follow a standard vaporliquid-solid (VLS) growth where Sn produced in situ is melted into Sn nanocrystal seeds on the SiO2 substrate and acts as a crystallization promoter for Si NR growth (Scheme 2 and Supporting Information, Figure S1). 42,52,53 SiH₄ can diffuse throughout the SiO2 matrix, diffuse into the Sn seed, and be catalytically decomposed to form elemental Si and H₂. The NRs are freed through HF etching, which simultaneously dissolved SiO₂ and Sn, leaving behind a suspension of hydridecapped Si NRs that can be functionalized with 1-dodecene through thermal hydrosilylation.

Sn has been shown to induce crystallization of Si at temperatures as low as 300–500 °C, well within the temperature range of the thermal disproportionation mechanism of HSQ (250–450 °C). ⁵⁴ As a result, highly crystalline Si NRs can be produced at much lower temperatures (450 °C) compared to synthesis of Si nanocrystals using HSQ without the presence of Sn (>1000 °C). ^{20,23} Additionally, the potential for alloying is extremely low due to large differences in lattice mismatch and the difference in the preferred crystal structure of thermodynamically stable Si (diamond cubic) and Sn (tetragonal, β -Sn). Therefore, any residual segregated Sn can be efficiently removed via HF etching without affecting the physical properties of the NRs.

Structural and Optical Properties of Si NRs Synthesized with a Sn Promoter. Si NRs were made in the presence of different molar concentrations of SnCl₄ ranging from 0.2 to 3.0%. The structural properties of NRs were studied through PXRD and Raman spectroscopy. PXRD patterns show that all synthesized NRs exhibit the diamond cubic structure indicative of crystalline Si (Figure 1A). Moreover, Bragg reflections corresponding to α -Sn, β -Sn, SnO₂, and SiO₂ impurities were not observed after the Si NRs were liberated from the SiO₂ matrix by HF etching, suggesting the growth and efficient etching of phase-pure Si NRs. To confirm the absence of microscopic impurities of Sn, EDX was used for composition analysis of dodecane-passivated Si NRs, which show no Sn (Supporting Information, Figure S2). Since the Si NRs are the only expected crystalline product, the influence of Sn on NR growth can be seen by comparing the PXRD patterns of pure HSQ to HSQ synthesized in the

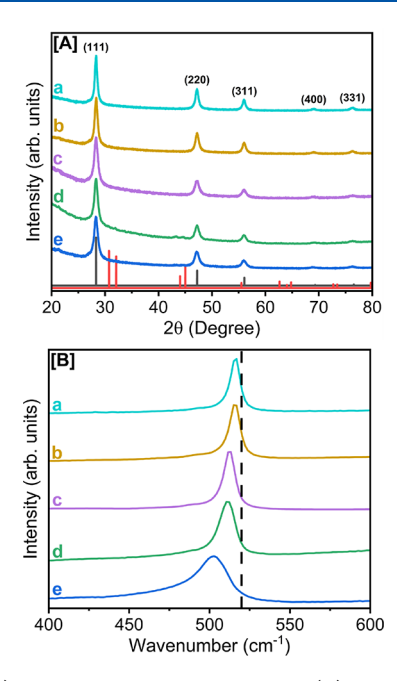


Figure 1. (A) PXRD diffraction patterns and (B) Raman spectra for Si NRs produced via thermal disproportionation of HSQ in the presence of (a) 3.0, (b) 1.0, (c) 0.5, (d) 0.35, and (e) 0.2% SnCl₄. ICCD-PDF overlays of diamond cubic Si (JCPDS 00-001-0971) and tetragonal β-Sn (JCPDS 00-001-0926) are shown as vertical solid red and black lines. The dashed vertical line in (B) indicates the bulk silicon Si–Si phonon mode for reference.

presence of SnCl₄, before and after annealing at 450 °C (Supporting Information, Figure S3). Prior to annealing, a single, broad peak at 21.5° can be observed for HSQ with and without SnCl₄ that can be attributed to amorphous SiO₂, suggesting the amorphous nature of the sample. 49 However, when SnCl₄ is present, high-intensity peaks were observed for both cubic Si and tetragonal β -tin, along with a broad amorphous peak of SiO2, indicating the growth and crystallization of Si NRs at 450 °C. However, peaks corresponding to diamond cubic Si were not observed in HSQ annealed at 450 °C without SnCl₄. Bragg reflections observed for Si NRs can be indexed to the diamond cubic crystal structure of Si (JCPDS 00-001-0971). This suggests that the presence of Sn is essential for NR growth at 450 °C. The crystallite sizes of the NRs synthesized with varying concentrations of SnCl₄ were calculated using the Scherrer formula and estimated to be 7.3 (0.2% SnCl₄), 7.9 (0.35% SnCl₄), 8.5 (0.5% SnCl₄), 10.0 (1.0% SnCl₄), and 11.5 nm (3.0% SnCl₄).⁴⁴ A noteworthy increase in crystallite size and crystallinity of phase-pure Si NRs was observed with increasing SnCl₄ concentration in HSQ (Figure 1A).

Raman spectra were recorded to probe the local bonding environment of Si NRs produced with SnCl₄ and compared to that of bulk Si (Figure 1B). The phonon mode of bulk crystalline Si–Si bonds produces a peak at 520 cm⁻¹, and for amorphous Si–Si bonds, this has been observed at 480–475 cm^{-1,55,56} In contrast, the peak position of the Si–Si phonon mode of Si NRs produced in the presence of the SnCl₄ promoter changes as follows: 502.8 (0.2% SnCl₄), 512.3 (0.35% SnCl₄), 513.3 (0.5% SnCl₄), 515.1 (1.0% SnCl₄), and 516.2 cm⁻¹ (3.0% SnCl₄). Si NRs show redshifted peaks from bulk Si owing to size confinement effects anticipated in NRs.^{57,58} Additionally, because of the decrease in the average

diameter, the peak positions of the Si–Si phonon mode are redshifted into a low-energy region and show significant tailing behavior specifically at lower SnCl₄ concentrations. This tailing effect can be attributed to higher ratios of undercoordinated surface Si atoms compared to fully coordinated core Si atoms. S5,59 As the NR diameter decreases, the number of undercoordinated Si atoms increases, giving rise to an asymmetric peak. This tailing behavior is also seen in semiconductor nanocrystals due to phonon confinement effects. No amorphous Si–Si shoulder is observed in any of the samples examined, indicating that the as-synthesized Si NRs are highly crystalline.

The morphology of the Si NRs was investigated through TEM. Si NRs produced from this route reveal a worm-like morphology of aggregated NRs consisting mostly of polycrystalline domains (Supporting Information, Figure S4). It is observed that smaller NRs exhibited more kinking, appearing as darker domains, potentially due to interbonding and the presence of crystal twinning defects, commonly seen in solution-based NR syntheses. 35,61 When these darker domains were examined with high-resolution TEM, it was confirmed that multiple lattices, usually two, are overlaying and interbonding with each other, providing crystal domains for the NRs to kink (Supporting Information, Figure S4). This defect is commonly observed in Si NRs produced with supercritical fluid-liquid-solid (SFLS) and solution-liquidsolid (SLS) growth methods in the presence of seed particles. ^{24,62} This phenomenon can occur due to several factors; however, it is most likely that kinking is influenced by changes in temperature during heating and cooling phases. 63,6 Additionally, kinking is more prevalent in Si NRs produced at high concentrations of SnCl₄. As previously discussed, these NRs, synthesized at 450 °C, were much larger than Si nanocrystals synthesized without a Sn promoter at 1100 °C. Elemental Sn can be produced as small, highly crystalline, pseudo-nanocrystals during annealing (Supporting Information, Figure S1). For Sn-promoted growth, the diameter of the NRs was seen to increase nearly linearly with the concentration of SnCl₄ (Supporting Information, Figure S5). Varying the concentrations of SnCl₄ resulted in average NR diameters of $7.69 \pm 0.86 \ (0.2\%), 7.97 \pm 0.95 \ (0.35\%), 8.18 \pm 1.12 \ (0.5\%),$ 11.85 ± 1.70 (1.0%), and 16.47 ± 3.14 nm (3.0%) for Si NRs (Figure 2A-E). It was also observed that at higher concentrations of SnCl₄ (1.0-3.0%), longer and more polydisperse Si NRs with 100-120 nm average lengths were produced, whereas at low concentrations of SnCl₄ (0.2–0.5%), shorter (50-80 nm) and more narrowly disperse Si NRs were obtained. This is likely due to higher concentrations of SnCl₄ producing larger, more polydisperse Sn seeds, leading to larger and more polydisperse NRs. 65,66 For Si NRs produced with 3.0 and 0.2% SnCl₄, SAED and HRTEM were used to estimate the d-spacing. SAED patterns show low-intensity concentric rings that can be indexed to the diamond cubic crystal structure of Si suggesting the polycrystallinity of the materials consistent with HRTEM. Both techniques agreed with a d-spacing of 3.13 Å (Figure 2F,I), which we attribute to the (111) plane of the diamond cubic Si, suggesting no alloying of Sn with Si consistent with the larger lattice mismatch.

FTIR spectroscopy provides valuable insight into the surface chemistry of the Si NRs produced with SiCl₄ as a promoter. The hydride-terminated Si NRs liberated from the SiO₂ matrix show peaks that can be attributed to Si–H bonds present on the NR surface (Figure 3a). There is a Si–H $_x$ (x = 1, 2, and 3)

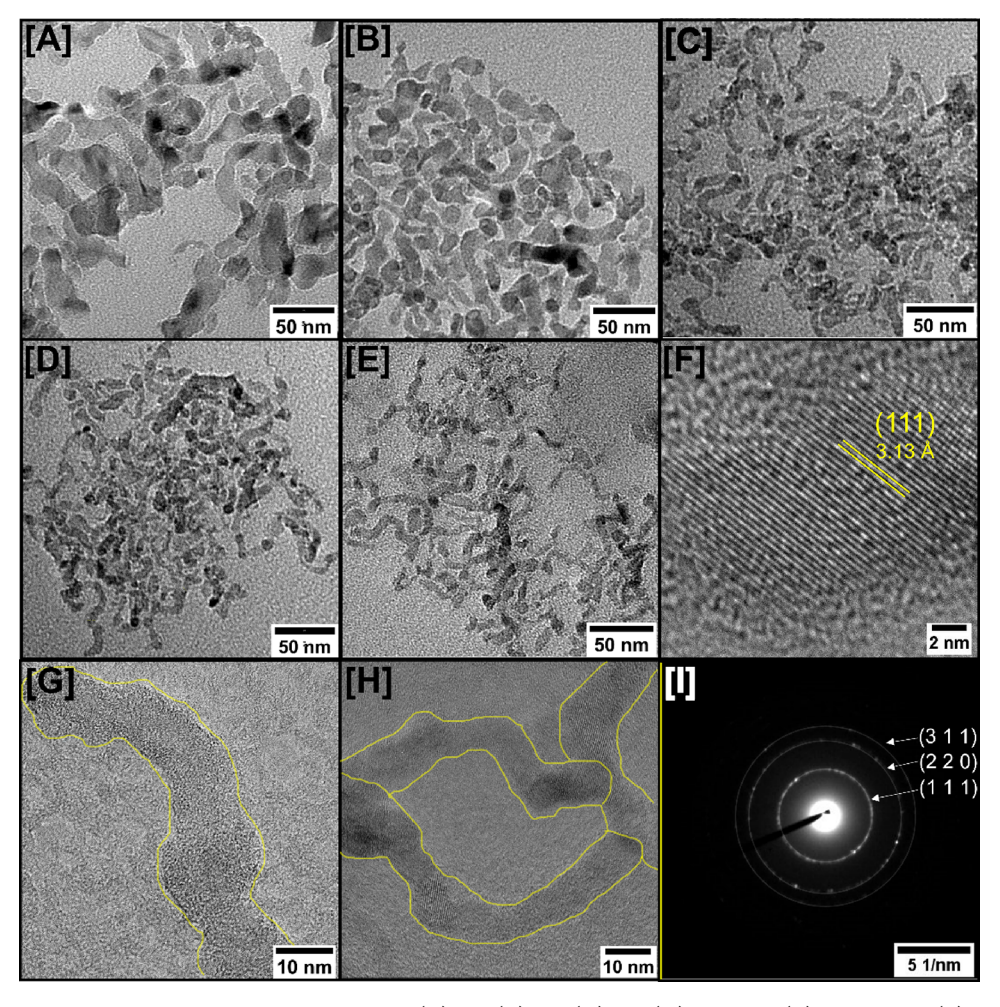


Figure 2. Low-resolution TEM images of Si NRs produced with (A) 3.0, (B) 1.0, (C) 0.5, (D) 0.35, and (E) 0.2% SnCl₄. (F) High-resolution TEM image of a single Si NR produced with 3.0% SnCl₄ showing a lattice spacing of 3.13 Å corresponding to the (111) plane of cubic Si. Higher-magnification images of Si NRs produced with (G) 3.0 and (H) 0.2% SnCl₄ along with (I) a representative SAED pattern of Si NRs produced with 3.0% SnCl₄. Guidelines provided for high-resolution TEM and SAED (G–I) for clarity.

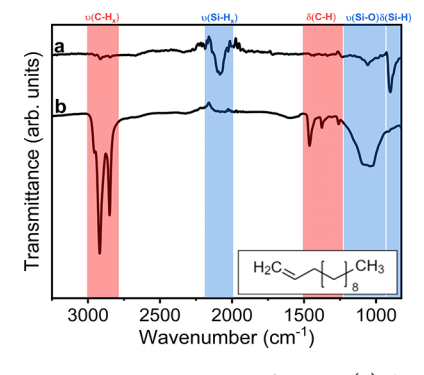


Figure 3. Representative FTIR spectra of Si NRs (a) directly after HF etching and (b) subsequent surface functionalization with 1-dodecene. The structure of 1-dodecene is shown as an inset.

stretching peak at 2084 cm⁻¹ along with a Si–H deformation peak at 899 cm⁻¹. Additionally, there is a Si–O stretching peak at 1061 cm⁻¹, which we attribute to minor surface oxidation upon exposure to air during handling. There are no apparent carbon-containing peaks except a small $C-H_x$ stretching peak due to residual ethanol from etching. It should be noted that, with appropriate care and atmosphere, oxidation can be minimized or completely avoided. After functionalization with

1-dodecene, the intensity of the Si–H vibrations significantly decreased along with the appearance of strong $C-H_x$ stretches (2800–2950 cm⁻¹) and deformation vibrations (1250–1500 cm⁻¹) indicating the successful removal of the hydride group and complexation with alkene ligands. Consistent with FTIR, an increase in colloidal stability of Si NRs in nonpolar solvents was noted after passivation with 1-dodecene.

To determine the effectiveness of HF etching and subsequent surface passivation with dodecane ligands, XPS was used (Figure 4 and Supporting Information, Figures S6 and S7). Si (2p) XPS spectra of dodecane-capped Si NRs showed two major peaks. The lowest-energy peak observed at 99.0–99.5 eV binding energies indicates Si⁰ species of the core NRs (Figure 4), which is consistent with the literature. ^{24,67,68} The absence of the Si⁰ peak shift to a higher-energy region rules out the presence of Si-Sn alloy impurities, which are highly unlikely to form due to large differences in lattice constants. During ligand exchange, the hydride-terminated surface of the NRs will decompose into surface silyl radicals, which can then interact with the double bond of 1-dodecene, forming a strong, covalently bound ligand, seen as a second major peak centered at 102.6 eV. 69,70 This peak can be attributed to Si-C bonding, suggesting the efficient surface functionalization with dodecane ligands. The high-energy

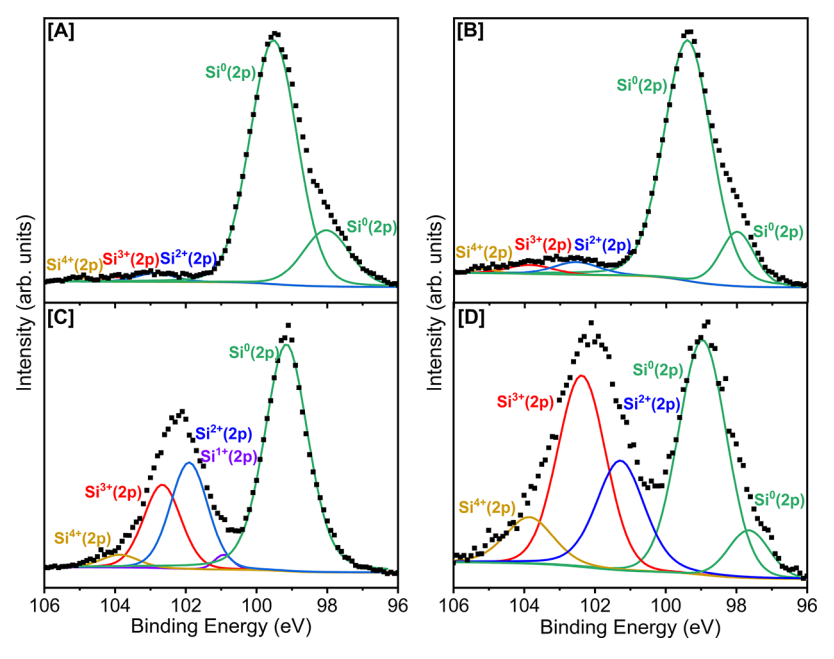


Figure 4. Si (2p) XPS spectra of Si NRs synthesized in the presence of (A) 3.0, (B) 1.0, (C) 0.35, and (D) 0.2% SnCl₄. The square symbols are raw spectral data, and the colored lines are fitted deconvolutions.

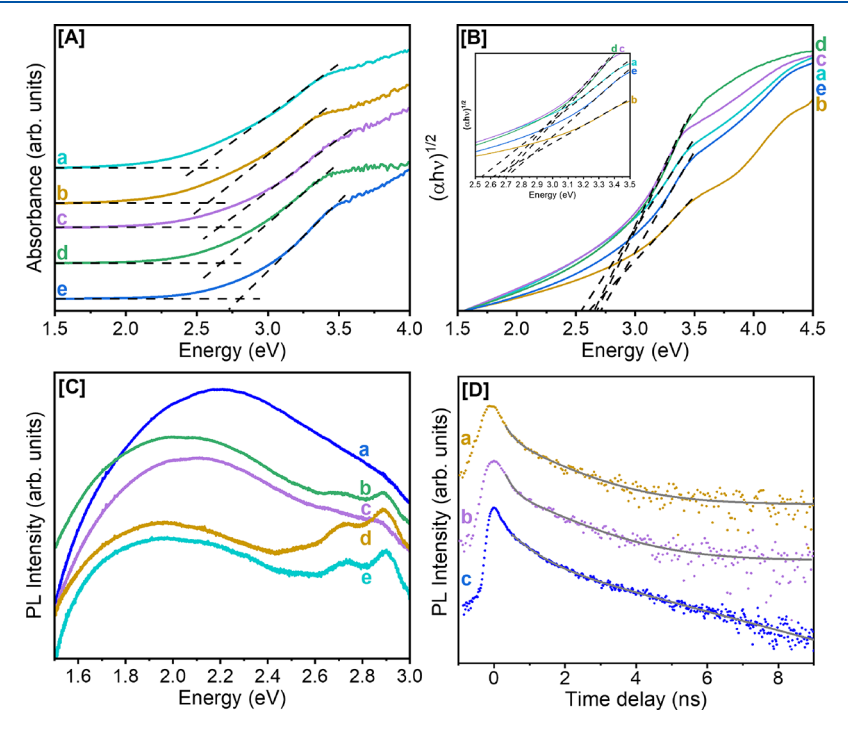


Figure 5. (A) Solid-state absorption spectra and (B) Tauc (indirect) plots of Si NRs synthesized in the presence of (a) 3.0, (b) 1.0, (c) 0.5, (d) 0.35, and (e) 0.2% SnCl₄. The inset in (B) shows a zoomed-in plot deconvoluting the energy gap measurements. (C) Solid-state PL spectra for Si NRs synthesized with (a) 0.2, (b) 0.35, (c) 0.5, (d) 1.0, and (e) 3.0% SnCl₄. (D) TRPL spectra obtained from Si NRs produced with (a) 1.0, (b) 0.5, and (c) 0.2% SnCl₄.

shoulder associated with this peak (Figure 4C,D) can be deconvoluted into multiple smaller peaks including Si^{1+} (100.8 eV), Si^{2+} (101.3–102.8 eV), Si^{3+} (102.3–103.9 eV), and Si^{4+} (103.9–105.0 eV) species, which can be attributed to various monoxides, dioxides, and suboxides of Si originating from minor surface oxidation. All peaks were seen to trend toward lower binding energies, by 0.5–1.1 eV, for smaller NRs produced with lower concentrations of $\mathrm{SnCl_4}$ and can be explained by the electronegativity difference in silicon and

carbon as well as surface charging effects, commonly observed in semiconductor nanomaterials, which are more prevalent for smaller NRs due to the higher ratio of surface-to-core atoms. 13,71,72

The relative intensity of the Si⁰ and the Si-C peaks can be compared with changes in the SnCl₄ concentration to gain insight into the core-to-surface Si⁰/Si-C ratio of NRs (Supporting Information, Figure S8). For NRs that were produced with a high concentration of SnCl₄, the Si⁰ peak is

much more intense than the Si–C peak, suggesting that the core-to-surface Si 0 /Si–C ratio is higher and the NRs are larger. As the concentration of SnCl $_4$ is decreased, the core-to-surface ratio and binding energy of Si decrease, which suggests that the NRs are decreasing in size. It is worth noting that the accuracy of this comparison is higher for thinner NRs as the penetration depth for Al K α sources is ~10 nm. This explains why the Si–C peak is considerably higher for smaller-diameter Si NRs produced at lower Sn concentrations (0.2–0.5%) compared to larger-diameter NRs produced at high Sn concentrations (1.0–3.0%).

Because the Si NRs have diameters (7.7-16.5 nm) larger or on par with the excitonic Bohr radius of bulk silicon, weak quantum confinement effects are expected. However, the variations in energy gaps can still be probed as the NR diameter approaches the confinement region and can be correlated with the SnCl₄ concentration. First, the energy gaps of Si NRs were probed using solid-state diffuse reflectance (converted to absorption using the Kubelka-Munk remission function) spectroscopy. 45,46 The solid-state absorption spectra of Si NRs show well-defined absorption onsets in the visible spectrum, 2.51-2.80 eV, for NRs produced with 0.2-3.0% SnCl₄, respectively (Figure 5A). Second, the band gaps were also probed using solution-state absorption spectroscopy.^{73–75} The solution absorption spectra of Si NRs show no excitonic peaks in the visible spectrum which, is typical for nanostructured Si. 20,24,27,76 The indirect energy gaps of Si NRs were probed using Tauc analysis and by plotting $(\alpha h\nu)^{1/2}$ vs energy. The energy gaps obtained from Tauc indirect plots indicate values from 2.54 to 2.70 eV for NRs produced with 0.2-3.0% SnCl₄ concentrations, respectively (Figure 5B). A systematic decrease in energy gaps with an increasing Sn concentration is clearly noted, which is consistent with the increase in the NR diameter at high Sn concentrations. In general, the solutionstate Tauc indirect analysis afforded slightly higher energy gaps compared to absorption onsets probed from solid-state diffuse reflectance spectroscopy (converted to absorption). However, both techniques are in good agreement with each other and show a decrease in energy gap with an increasing SnCl₄ concentration (Supporting Information, Figure S9). In addition, both techniques show a large blueshift in energy gaps compared to bulk Si (1.1 eV)⁷⁷ and an increase in energy gaps with a decrease in the NR diameter, consistent with other literature reports of Si NRs produced by different methods. 26,27

PL from Si NRs can only be probed after HF etching and surface passivation with dodecane. In contrast, NRs embedded in the SiO₂/Sn matrix show no appreciable emission. We attribute this to the presence of metallic Sn seeds, which can act as PL quenchers, a behavior reported in many Si nanocrystals. 24,35 Si NRs liberated from annealed HSQ consistently showed wide-band emission across the visible spectrum. Room-temperature PL spectra of representative Si NR samples synthesized using varying SnCl₄ contents are shown in Figure 5C. The main PL peak positions obtained from multi-Gaussian fits are plotted versus SnCl₄ concentration in Supporting Information, Figure S9 along with the absorption onsets and Tauc indirect gaps obtained from the solid- and solution-state measurements, respectively. PL peak energies were observed to range from 2.20 to 1.95 eV, consistently redshifting in response to progressively decreasing the degrees of confinement correlated with an increasing SnCl₄ concentration (0.2-3.0%) and the associated increases in the NR diameter (7.7-16.5 nm). This systematic confinementrelated redshift relative to the $SnCl_4$ content and NR diameter is also in agreement with the trend seen in the absorption edge dependence (Figure 5A). The dominant emission peaks for each sample were found to be generally broad and significantly shifted in comparison to their corresponding absorption edge, having an FWHM on the order of 800 meV and an average shift of 592 meV.

While the diameters of these Si NRs are comparable to (or slightly larger than) the exciton Bohr radius of bulk silicon, the observed high absorption edges and emission peak energies are consistent with previous reports on Si NRs having similar diameters. 35,78,79 The significantly blueshifted emission peaks (when compared with the bulk Si band gap of $\sim 1.1 \text{ eV}$)⁷⁷ seen here and in numerous other Si nanocrystal and NR systems are typically ascribed to confinement effects or surface defects present across the larger surface area of the material.⁸⁰⁻⁸³ TRPL measurements performed on select Si NR samples (Figure 5D) indicate biexponential decays with fast/slow time constants of 0.19-0.57 ns/1.32-2.57 ns for an $\sim 100 \text{ meV}$ wide spectral region around the main peak, a much smaller timescale than the comparatively slow μ s-order luminescence lifetime characteristic of confined Si emission.^{84,85} Such short carrier lifetimes have been attributed to fast recombination channels within surface-related defects; 84,86 thus, such surface states may, in part, be responsible for the broad emission observed in this study.

Barring phonon-assisted indirect Si transitions, a potential absorption/re-emission system to further address the diameterassociated shifting, broadness, and relatively large Stokes shift of the main emission can be ascertained upon close inspection of the NR morphology. As shown in Figure 2, there is large diameter variance across individual NRs. The high confinement (smallest diameter) sections of the rods are likely the main progenitors of the absorption/emission process, having strong absorption and emission while still showing generalized size dependence along with an increasing Sn concentration. The majority of the photons generated inside these areas of the NRs are then trapped inside the structure due to the high refractive index, sequentially being absorbed and re-emitted by the lower confinement (larger diameter) regions until either emanating from the ends of the rods or being lost to nonradiative recombination. Ultimately, the emission from these low confinement domains (with correspondingly lower transition energies) will likely dominate the PL spectra in accordance with the overall average rod diameter.

The origin of the omnipresent peaks located at the highenergy sides of the measured spectra (visible in Figure 5C) is more opaque, as peaks in this vicinity could be attributed to a variety of potential sources. ^{26,80,82,83,86,87} Some suggested possibilities as to their cause include the addition of independent recombination channels arising from surface/ interface defects associated with incomplete or alternate functionalization mechanisms. If in some cases the irregularly shaped NRs do not reach 100% passivation, unrecognized peaks such as these could be a consequence of resulting factors such as oxidation ^{26,82,83} or other unidentified surface states, ^{80,86,87} but further investigation is required in order to pinpoint the exact origin of these luminescence peaks and will be discussed elsewhere.

CONCLUSIONS

In conclusion, we have successfully produced highly crystalline Si NRs using SnCl₄ as a simple molecular crystallization

promoter and HSQ as a precursor at a considerably lower temperature (450 °C) than those (>1000 °C) typically used in the synthesis of Si nanocrystals and eliminating the added complexity and requirement of preformed promoters like metal nanocrystals. 21,35,40,52,65 The amount of SnCl₄ added to HSQ, 0.2-3.0%, can be used to directly control the diameter (7.7-16.5 nm) and length (50–120 nm) of Si NRs. The addition of SnCl₄ in an initial step prior to HSQ gelation allows the homogeneous distribution of SnCl₄ in the HSQ matrix promoting the growth of smaller-diameter Si NRs. PXRD and TEM studies reveal that NRs show high crystallinity, diamond cubic structure, and variable diameters that can be correlated to the concentration of SnCl₄. A shift of Bragg reflections was not observed due to larger lattice mismatch of Si and Sn, which is consistent with the growth of phase-pure Si NRs. 35,52,66 Raman spectra show broadening and redshifting of the Si-Si phonon mode from the bulk Si and tailing toward lower energies as the NR dimeter is decreased, which we attribute to increased size confinement effects in smaller NRs. The FTIR spectra of Si NRs functionalized with alkanes show the disappearance of the Si-H vibrations and appearance of C-H vibrations, consistent with the increased colloidal stability of dodecane-coated Si NRs. This passivation was further confirmed by XPS where the intensity ratio of the Si-C to core Si⁰ peaks provides pseudo-quantitative clues regarding the NR diameter. Solid-state and solution-state absorption spectra of Si NRs show well-defined absorption onsets (2.51-2.80 eV and 2.48-2.70 eV, respectively) in the visible spectrum, which are larger than bulk Si indicating strong size confinement effects in NRs. 26,27,88 Photoluminescence from Si NRs shows nanosecond lifetimes and broad (~0.8 eV) peaks that redshift with an increasing rod diameter. Peak emission occurs consistently at ~0.6 eV below the absorption onset, suggesting self-absorption and re-emission occurring at lower confinement regions within the NRs. This new synthetic methodology provides an efficient approach for low-cost fabrication of size-confined Si NRs with high crystallinity, variable diameters, and tunable absorption and PL properties for optoelectronic, charge storage, and photocatalytic applications. Specific studies to test this premise are currently underway.

ASSOCIATED CONTENT

Supporting Information

The Supporting Information is available free of charge at https://pubs.acs.org/doi/10.1021/acs.jpcc.3c01308.

Literature reports on Si NRs and corresponding PL peak maxima, details of the different synthetic pathways and amounts of precursors used in the synthesis of HSQ and Si NRs, PXRD patterns of HSQ annealed under different atmospheric conditions before and after annealing, EDX spectra and HRTEM images of Si NRs, plots of SnCl₄ concentration versus nanorod diameter and ratio of XPS peaks, XPS survey scans of Si NRs, and comparison of solid-state and solution-state energy gaps versus solid-state PL peak positions (PDF)

AUTHOR INFORMATION

Corresponding Author

Indika U. Arachchige – Department of Chemistry, Virginia Commonwealth University, Richmond, Virginia 23284-2006, *United States;* orcid.org/0000-0001-6025-5011; Email: iuarachchige@vcu.edu

Authors

Griffin C. Spence – Department of Chemistry, Virginia Commonwealth University, Richmond, Virginia 23284-2006, United States

Rachel C. Barbieri – Department of Chemistry, Virginia Commonwealth University, Richmond, Virginia 23284-2006, United States

David Pate — Department of Electrical and Computer Engineering, Virginia Commonwealth University, Richmond, Virginia 23220, United States; orcid.org/0000-0002-1497-651X

Lisa S. Graves – Department of Chemistry, Virginia Commonwealth University, Richmond, Virginia 23284-2006, United States

Ümit Özgür – Department of Electrical and Computer Engineering, Virginia Commonwealth University, Richmond, Virginia 23220, United States

Complete contact information is available at: https://pubs.acs.org/10.1021/acs.jpcc.3c01308

Author Contributions

The manuscript was written through contributions of all authors. All authors have given approval to the final version of the manuscript.

Notes

The authors declare no competing financial interest.

ACKNOWLEDGMENTS

The authors gratefully acknowledge financial support from the US National Science Foundation DMR-2211606 award and the Department of Chemistry at Virginia Commonwealth University.

REFERENCES

- (1) Salam Mahmood, A.; Venkatakrishnan, K.; Tan, B. Silicon Nano Network p—n Sandwich Solar Cell. Sol. Energy Mater. Sol. Cells 2013, 115. 58–63.
- (2) Crisp, R. W.; Kirkwood, N.; Grimaldi, G.; Kinge, S.; Siebbeles, L. D. A.; Houtepen, A. J. Highly Photoconductive InP Quantum Dots Films and Solar Cells. ACS Appl. Energy Mater. 2018, 1, 6569–6576.
- (3) Kamat, P. V. Quantum Dot Solar Cells. Semiconductor Nanocrystals as Light Harvesters. J. Phys. Chem. C 2008, 112, 18737–18753.
- (4) Ji, X.; Wang, H.; Song, B.; Chu, B.; He, Y. Silicon Nanomaterials for Biosensing and Bioimaging Analysis. *Front. Chem.* **2018**, *6*, 38.
- (5) Fan, J.; Chu, P. K. Group IV Nanoparticles: Synthesis, Properties, and Biological Applications. *Small* **2010**, *6*, 2080–2098.
- (6) Kim, H.; Seo, M.; Park, M.-H.; Cho, J. A Critical Size of Silicon Nano-Anodes for Lithium Rechargeable Batteries. *Angew. Chem., Int. Ed.* **2010**, *49*, 2146–2149.
- (7) Yang, Y.; Yuan, W.; Kang, W.; Ye, Y.; Yuan, Y.; Qiu, Z.; Wang, C.; Zhang, X.; Ke, Y.; Tang, Y. Silicon-Nanoparticle-Based Composites for Advanced Lithium-Ion Battery Anodes. *Nanoscale* **2020**, *12*, 7461–7484.
- (8) Shin, H.-J.; Hwang, J.-Y.; Kwon, H. J.; Kwak, W.-J.; Kim, S.-O.; Kim, H.-S.; Jung, H.-G. Sustainable Encapsulation Strategy of Silicon Nanoparticles in Microcarbon Sphere for High-Performance Lithium-Ion Battery Anode. ACS Sustainable Chem. Eng. 2020, 8, 14150—14158.
- (9) Franklin, A. D. Nanomaterials in Transistors: From High-Performance to Thin-Film Applications. *Science* **2015**, 349, No. aab2750.

- (10) Jung, S. M.; Kang, H. L.; Won, J. K.; Kim, J.; Hwang, C.; Ahn, K.; Chung, I.; Ju, B.-K.; Kim, M.-G.; Park, S. K. High-Performance Quantum Dot Thin-Film Transistors with Environmentally Benign Surface Functionalization and Robust Defect Passivation. ACS Appl. Mater. Interfaces 2018, 10, 3739–3749.
- (11) Tallur, S.; Bhave, S. A. A Silicon Electromechanical Photo-detector. *Nano Lett.* **2013**, *13*, 2760–2765.
- (12) Shen, D. S.; Conde, J. P.; Chu, V.; Aljishi, S.; Liu, J. Z.; Wagner, S. Amorphous Silicon-Germanium Thin-Film Photodetector Array. *IEEE Electron Device Lett.* **1992**, *13*, 5–7.
- (13) Esteves, R. J. A.; Ho, M. Q.; Arachchige, I. U. Nanocrystalline Group IV Alloy Semiconductors: Synthesis and Characterization of Ge1–XSnx Quantum Dots for Tunable Bandgaps. *Chem. Mater.* **2015**, 27, 1559–1568.
- (14) Spera, D. Z.; Arachchige, I. U. Improved Surface Passivation of Colloidal Ge1–XSnx Nanoalloys through Amorphous SiO2 Shell Growth. *J. Phys. Chem. C* **2022**, *126*, 9862–9874.
- (15) Reiss, P.; Carrière, M.; Lincheneau, C.; Vaure, L.; Tamang, S. Synthesis of Semiconductor Nanocrystals, Focusing on Nontoxic and Earth-Abundant Materials. *Chem. Rev.* **2016**, *116*, 10731–10819.
- (16) Barbieri, R. C.; Ding, K.; Özgür, Ü.; Arachchige, I. U. Solution-Processed Ge1–x Snx Alloy Nanocrystal Thin Films with High Electrical Conductivity and Tunable Energy Gaps. *Chem. Mater.* **2021**, 33, 6897–6908.
- (17) Zhu, G.; Chao, D.; Xu, W.; Wu, M.; Zhang, H. Microscale Silicon-Based Anodes: Fundamental Understanding and Industrial Prospects for Practical High-Energy Lithium-Ion Batteries. *ACS Nano* **2021**, *15*, 15567–15593.
- (18) Lozac'h, M.; Švrček, V.; Askari, S.; Mariotti, D.; Ohashi, N.; Koganezawa, T.; Miyadera, T.; Matsubara, K. Semiconducting Silicon-Tin Alloy Nanocrystals with Direct Bandgap Behavior for Photovoltaic Devices. *Mater. Today Energy* **2018**, *7*, 87–97.
- (19) Švrček, V.; Mariotti, D.; Blackley, R. A.; Zhou, W. Z.; Nagai, T.; Matsubara, K.; Kondo, M. Semiconducting Quantum Confined Silicon—Tin Alloyed Nanocrystals Prepared by Ns Pulsed Laser Ablation in Water. *Nanoscale* **2013**, *5*, 6725–6730.
- (20) Hessel, C. M.; Reid, D.; Panthani, M. G.; Rasch, M. R.; Goodfellow, B. W.; Wei, J.; Fujii, H.; Akhavan, V.; Korgel, B. A. Synthesis of Ligand-Stabilized Silicon Nanocrystals with Size-Dependent Photoluminescence Spanning Visible to Near-Infrared Wavelengths. *Chem. Mater.* **2012**, *24*, 393–401.
- (21) Terada, S.; Xin, Y.; Saitow, K. Cost-Effective Synthesis of Silicon Quantum Dots. Chem. Mater. 2020, 32, 8382-8392.
- (22) Fang, R.; Chen, K.; Yin, L.; Sun, Z.; Li, F.; Cheng, H.-M. The Regulating Role of Carbon Nanotubes and Graphene in Lithium-Ion and Lithium—Sulfur Batteries. *Adv. Mater.* **2019**, *31*, 1800863.
- (23) Clark, R. J.; Aghajamali, M.; Gonzalez, C. M.; Hadidi, L.; Islam, M. A.; Javadi, M.; Mobarok, M. H.; Purkait, T. K.; Robidillo, C. J. T.; Sinelnikov, R.; Thiessen, A. N.; Washington, J.; Yu, H.; Veinot, J. G. C. From Hydrogen Silsesquioxane to Functionalized Silicon Nanocrystals. *Chem. Mater.* **2017**, *29*, 80–89.
- (24) Lu, X.; Hessel, C. M.; Yu, Y.; Bogart, T. D.; Korgel, B. A. Colloidal Luminescent Silicon Nanorods. *Nano Lett.* **2013**, *13*, 3101–3105.
- (25) Heinrich, J. L.; Curtis, C. L.; Credo, G. M.; Sailor, M. J.; Kavanagh, K. L. Luminescent Colloidal Silicon Suspensions from Porous Silicon. *Science* **1992**, 255, 66–68.
- (26) Li, R.; Zhang, X.; Zhang, D.; Zhang, Y.; Xiang, G. Optical Properties and Quantum Confinement in Ultrafine Single Crystal Silicon Nanowires Synthesized by Thermal Evaporation without Catalyst. RSC Adv. 2013, 3, 15982–15986.
- (27) Dixit, S.; Shukla, A. K. Optical Properties of Lonsdaleite Silicon Nanowires: A Promising Material for Optoelectronic Applications. *J. Appl. Phys.* **2018**, 123, 224301.
- (28) Zhang, H.; Kikuchi, N.; Ohshima, N.; Kajisa, T.; Sakata, T.; Izumi, T.; Sone, H. Design and Fabrication of Silicon Nanowire-Based Biosensors with Integration of Critical Factors: Toward Ultrasensitive Specific Detection of Biomolecules. *ACS Appl. Mater. Interfaces* **2020**, *12*, 51808–51819.

- (29) Cao, A.; Sudhölter, E. J. R.; de Smet, L. C. P. M. Silicon Nanowire-Based Devices for Gas-Phase Sensing. *Sensors* **2014**, *14*, 245–271.
- (30) Kondratev, V. M.; Morozov, I. A.; Vyacheslavova, E. A.; Kirilenko, D. A.; Kuznetsov, A.; Kadinskaya, S. A.; Nalimova, S. S.; Moshnikov, V. A.; Gudovskikh, A. S.; Bolshakov, A. D. Silicon Nanowire-Based Room-Temperature Multi-Environment Ammonia Detection. *ACS Appl. Nano. Mater.* **2022**, *5*, 9940–9949.
- (31) El-Bashar, R.; Hussein, M.; Hegazy, S. F.; Badr, Y.; Rahman, B. M. A.; Grattan, K. T. v.; Hameed, M.; Farhat, O.; Obayya, S. S. A. Electrical Performance of Efficient Quad-Crescent-Shaped Si Nanowire Solar Cell. Sci. Rep. 2022, 12, 48.
- (32) Morales, M. A.; Lieber, C. A. Laser Ablation Method for the Synthesis of Crystalline Semiconductor Nanowires. *Science* **1998**, 279, 208–211.
- (33) Niu, J.; Sha, J.; Yang, D. Silicon Nanowires Fabricated by Thermal Evaporation of Silicon Monoxide. *Phys. E* **2004**, *23*, 131–134.
- (34) Richter, G.; Hillerich, K.; Gianola, D. S.; Mönig, R.; Kraft, O.; Volkert, C. A. Ultrahigh Strength Single Crystalline Nanowhiskers Grown by Physical Vapor Deposition. *Nano Lett.* **2009**, *9*, 3048–3052.
- (35) Heitsch, A. T.; Hessel, C. M.; Akhavan, V. A.; Korgel, B. A. Colloidal Silicon Nanorod Synthesis. *Nano Lett.* **2009**, *9*, 3042–3047.
- (36) Wendisch, F. J.; Rey, M.; Vogel, N.; Bourret, G. R. Large-Scale Synthesis of Highly Uniform Silicon Nanowire Arrays Using Metal-Assisted Chemical Etching. *Chem. Mater.* **2020**, *32*, 9425–9434.
- (37) Heitsch, T. A.; Fanfair, D. D.; Tuan, H.-Y.; Korgel, A. B. Solution—Liquid—Solid (SLS) Growth of Silicon Nanowires. *J. Am. Chem. Soc.* **2008**, *130*, 5436—5437.
- (38) Yuan, F.-W.; Yang, H.-J.; Tuan, H.-Y. Seeded Silicon Nanowire Growth Catalyzed by Commercially Available Bulk Metals: Broad Selection of Metal Catalysts, Superior Field Emission Performance, and Versatile Nanowire/Metal Architectures. *J. Mater. Chem.* **2011**, 21, 13793–13800.
- (39) Gebavi, H.; Ristić, D.; Baran, N.; Marciuš, M.; Gašparić, V.; Syed, K.; Ivanda, M. Development of Silicon Nanowires Based on Ag-Au Metal Alloy Seed System for Sensing Technologies. *Sens. Actuators, A* **2021**, 331, No. 112931.
- (40) Rathi, S. J.; Jariwala, B. N.; Beach, J. D.; Stradins, P.; Taylor, P. C.; Weng, X.; Ke, Y.; Redwing, J. M.; Agarwal, S.; Collins, R. T. Tin-Catalyzed Plasma-Assisted Growth of Silicon Nanowires. *J. Phys. Chem. C* 2011, *115*, 3833–3839.
- (41) Jeon, M.; Uchiyama, H.; Kamisako, K. Characterization of Tin-Catalyzed Silicon Nanowires Synthesized by the Hydrogen Radical-Assisted Deposition Method. *Mater. Lett.* **2009**, *63*, 246–248.
- (42) Mullane, E.; Kennedy, T.; Geaney, H.; Dickinson, C.; Ryan, K. M. Synthesis of Tin Catalyzed Silicon and Germanium Nanowires in a Solvent–Vapor System and Optimization of the Seed/Nanowire Interface for Dual Lithium Cycling. *Chem. Mater.* **2013**, *25*, 1816–1822.
- (43) Tauc, J.; Grigorovici, R.; Vancu, A. Optical Properties and Electronic Structure of Amorphous Germanium. *Phys. Status Solidi* **1966**, 15, 627–637.
- (44) Borchert, H.; Shevchenko, E. v.; Robert, A.; Mekis, I.; Kornowski, A.; Grübel, G.; Weller, H. Determination of Nanocrystal Sizes: A Comparison of TEM, SAXS, and XRD Studies of Highly Monodisperse CoPt3 Particles. *Langmuir* **2005**, *21*, 1931–1936.
- (45) Tsuge, A.; Uwamino, Y.; Ishizuka, T.; Suzuki, K. Quantitative Analysis of Powdery Sample by Diffuse Reflectance Infrared Fourier Transform Spectrometry: Determination of the α Component in Silicon Nitride. *Appl. Spectrosc.* **1991**, *45*, 1377–1380.
- (46) Nowak, M.; Kauch, B.; Szperlich, P. Determination of Energy Band Gap of Nanocrystalline SbSI Using Diffuse Reflectance Spectroscopy. *Rev. Sci. Instrum.* **2009**, *80*, No. 046107.
- (47) Omer, A. I. M. Tin Ethoxide and Related Compounds. Ph.D. Dissertation, University of Khartoum, Khartoum State, Sudan, 2000. (48) Baney, R. H.; Itoh, M.; Sakakibara, A.; Suzuki, T. Silsesquioxanes. *Chem. Rev.* **1995**, *95*, 1409–1430.

- (49) Hessel, C. M.; Henderson, E. J.; Veinot, J. G. C. Hydrogen Silsesquioxane: A Molecular Precursor for Nanocrystalline Si–SiO₂ Composites and Freestanding Hydride-Surface-Terminated Silicon Nanoparticles. *Chem. Mater.* **2006**, *18*, 6139–6146.
- (50) Zhou, J.; Huang, J.; Chen, H.; Samanta, A.; Linnros, J.; Yang, Z.; Sychugov, I. Low-Cost Synthesis of Silicon Quantum Dots with Near-Unity Internal Quantum Efficiency. *J. Phys. Chem. Lett.* **2021**, 12, 8909–8916.
- (51) Olynick, D. L.; Cord, B.; Schipotinin, A.; Ogletree, D. F.; Schuck, P. J. Electron-Beam Exposure Mechanisms in Hydrogen Silsesquioxane Investigated by Vibrational Spectroscopy and *in Situ* Electron-Beam-Induced Desorption. *J. Vac. Sci. Technol., B* **2010**, 28, 581–587.
- (52) Chockla, A. M.; Klavetter, K. C.; Mullins, C. B.; Korgel, B. A. Tin-Seeded Silicon Nanowires for High Capacity Li-Ion Batteries. *Chem. Mater.* **2012**, *24*, 3738–3745.
- (53) Wagner, R. S.; Ellis, W. C. Vapor-Liquid-Solid Mechanism of Single Crystal Growth. *Appl. Phys. Lett.* **1964**, *4*, 89–90.
- (54) Neimash, V.; Poroshin, V.; Shepeliavyi, P.; Yukhymchuk, V.; Melnyk, V.; Kuzmich, A.; Makara, V.; Goushcha, A. O. Tin Induced A-Si Crystallization in Thin Films of Si-Sn Alloys. *J. Appl. Phys.* **2013**, *114*, 213104.
- (55) Yogi, P.; Tanwar, M.; Saxena, S. K.; Mishra, S.; Pathak, D. K.; Chaudhary, A.; Sagdeo, P. R.; Kumar, R. Quantifying the Short-Range Order in Amorphous Silicon by Raman Scattering. *Anal. Chem.* **2018**, 90, 8123–8129.
- (56) Parker, J. H.; Feldman, D. W.; Ashkin, M. Raman Scattering by Silicon and Germanium. *Phys. Rev.* **1967**, *155*, 712–714.
- (57) Faraci, G.; Gibilisco, S.; Russo, P.; Pennisi, A. R.; la Rosa, S. Modified Raman Confinement Model for Si Nanocrystals. *Phys. Rev. B* **2006**, 73, 33307.
- (58) Gao, Y.; Zhao, X.; Yin, P.; Gao, F. Size-Dependent Raman Shifts for Nanocrystals. Sci. Rep. 2016, 6, 20539.
- (59) Khoo, K. H.; Zayak, A. T.; Kwak, H.; Chelikowsky, J. R. First-Principles Study of Confinement Effects on the Raman Spectra of Si Nanocrystals. *Phys. Rev. Lett.* **2010**, *105*, No. 115504.
- (60) Paillard, V.; Puech, P.; Laguna, M. A.; Carles, R.; Kohn, B.; Huisken, F. Improved One-Phonon Confinement Model for an Accurate Size Determination of Silicon Nanocrystals. *J. Appl. Phys.* **1999**, *86*, 1921–1924.
- (61) Davidson, F. M.; Lee, D. C.; Fanfair, D. D.; Korgel, B. A. Lamellar Twinning in Semiconductor Nanowires. *J. Phys. Chem. C* **2007**, *111*, 2929–2935.
- (62) He, Z.; Nguyen, H. T.; Duc Toan, L.; Pribat, D. A Detailed Study of Kinking in Indium-Catalyzed Silicon Nanowires. *CrystEng-Comm* **2015**, 17, 6286–6296.
- (63) Madras, P.; Dailey, E.; Drucker, J. Kinetically Induced Kinking of Vapor-Liquid-Solid Grown Epitaxial Si Nanowires. *Nano Lett.* **2009**, *9*, 3826–3830.
- (64) Vlassov, S.; Oras, S.; Polyakov, B.; Butanovs, E.; Kyritsakis, A.; Zadin, V. Kinking in Semiconductor Nanowires: A Review. *Cryst. Growth Des.* **2022**, 22, 871–892.
- (65) Al-Taay, H. F.; Mahdi, M. A.; Parlevliet, D.; Jennings, P. Controlling the Diameter of Silicon Nanowires Grown Using a Tin Catalyst. *Mater. Sci. Semicond. Process.* **2013**, *16*, 15–22.
- (66) Meshram, N.; Kumbhar, A.; Dusane, R. O. Synthesis of Silicon Nanowires Using Tin Catalyst by Hot Wire Chemical Vapor Processing. *Mater. Res. Bull.* **2013**, 48, 2254–2258.
- (67) Yilbas, B. S.; Salhi, B.; Yousaf, M. R.; Al-Sulaiman, F.; Ali, H.; Al-Aqeeli, N. Surface Characteristics of Silicon Nanowires/Nanowalls Subjected to Octadecyltrichlorosilane Deposition and n-Octadecane Coating. *Sci. Rep.* **2016**, *6*, 38678.
- (68) Veerbeek, J.; Steen, R.; Vijselaar, W.; Rurup, W. F.; Korom, S.; Rozzi, A.; Corradini, R.; Segerink, L.; Huskens, J. Selective Functionalization with PNA of Silicon Nanowires on Silicon Oxide Substrates. *Langmuir* **2018**, *34*, 11395–11404.
- (69) Yang, Z.; Iqbal, M.; Dobbie, A. R.; Veinot, J. G. C. Surface-Induced Alkene Oligomerization: Does Thermal Hydrosilylation

- Really Lead to Monolayer Protected Silicon Nanocrystals? J. Am. Chem. Soc. 2013, 135, 17595–17601.
- (70) Holm, J.; Roberts, J. T. Thermally Induced Hydrosilylation at Deuterium-Terminated Silicon Nanoparticles: An Investigation of the Radical Chain Propagation Mechanism. *Langmuir* **2009**, *25*, 7050–7056
- (71) Kalebaila, K. K.; Georgiev, D. G.; Brock, S. L. Synthesis and Characterization of Germanium Sulfide Aerogels. *J. Non-Cryst. Solids* **2006**, 352, 232–240.
- (72) Yu, Y.; Rowland, C. E.; Schaller, R. D.; Korgel, B. A. Synthesis and Ligand Exchange of Thiol-Capped Silicon Nanocrystals. *Langmuir* **2015**, *31*, 6886–6893.
- (73) Aldakov, D.; Chappaz-Gillot, C.; Salazar, R.; Delaye, V.; Welsby, K. A.; Ivanova, V.; Dunstan, P. R. Properties of Electro-deposited CuSCN 2D Layers and Nanowires Influenced by Their Mixed Domain Structure. *J. Phys. Chem. C* **2014**, *118*, 16095–16103.
- (74) Ganguly, S.; Kazem, N.; Carter, D.; Kauzlarich, S. M. Colloidal Synthesis of an Exotic Phase of Silicon: The BC8 Structure. *J. Am. Chem. Soc.* **2014**, *136*, 1296–1299.
- (75) Arachchige, I. U.; Kanatzidis, M. G. Anomalous Band Gap Evolution from Band Inversion in Pb1–xSnxTe Nanocrystals. *Nano Lett.* **2009**, *9*, 1583–1587.
- (76) Pringle, T. A.; Hunter, K. I.; Brumberg, A.; Anderson, K. J.; Fagan, J. A.; Thomas, S. A.; Petersen, R. J.; Sefannaser, M.; Han, Y.; Brown, S. L.; Kilin, D. S.; Schaller, R. D.; Kortshagen, U. R.; Boudjouk, P. R.; Hobbie, E. K. Bright Silicon Nanocrystals from a Liquid Precursor: Quasi-Direct Recombination with High Quantum Yield. ACS Nano 2020, 14, 3858–3867.
- (77) Macfarlane, G. G.; McLean, T. P.; Quarrington, J. E.; Roberts, V. Fine Structure in the Absorption-Edge Spectrum of Si. *Phys. Rev.* **1958**, *111*, 1245–1254.
- (78) Zhang, Y. F.; Tang, Y. H.; Peng, H. Y.; Wang, N.; Lee, C. S.; Bello, I.; Lee, S. T. Diameter Modification of Silicon Nanowires by Ambient Gas. *Appl. Phys. Lett.* **1999**, *75*, 1842–1844.
- (79) Lu, S.; Wu, B.; Sun, Y.; Cheng, Y.; Liao, F.; Shao, M. Photoluminescence of Pure Silicon Quantum Dots Embedded in an Amorphous Silica Wire Array. *J. Mater. Chem. C Mater.* **2017**, *5*, 6713–6717.
- (80) Nolan, M.; O'Callaghan, S.; Fagas, G.; Greer, J. C.; Frauenheim, T. Silicon Nanowire Band Gap Modification. *Nano Lett.* **2007**, *7*, 34–38.
- (81) Song, B.; Zhong, Y.; Wu, S.; Chu, B.; Su, Y.; He, Y. One-Dimensional Fluorescent Silicon Nanorods Featuring Ultrahigh Photostability, Favorable Biocompatibility, and Excitation Wavelength-Dependent Emission Spectra. J. Am. Chem. Soc. 2016, 138, 4824–4831.
- (82) Qi, J.; White, J. M.; Belcher, A. M.; Masumoto, Y. Optical Spectroscopy of Silicon Nanowires. *Chem. Phys. Lett.* **2003**, 372, 763–766.
- (83) Yu, D. P.; Bai, Z. G.; Ding, Y.; Hang, Q. L.; Zhang, H. Z.; Wang, J. J.; Zou, Y. H.; Qian, W.; Xiong, G. C.; Zhou, H. T.; Feng, S. Q. Nanoscale Silicon Wires Synthesized Using Simple Physical Evaporation. *Appl. Phys. Lett.* **1998**, 72, 3458–3460.
- (84) Dasog, M.; Yang, Z.; Regli, S.; Atkins, T. M.; Faramus, A.; Singh, M. P.; Muthuswamy, E.; Kauzlarich, S. M.; Tilley, R. D.; Veinot, J. G. C. Chemical Insight into the Origin of Red and Blue Photoluminescence Arising from Freestanding Silicon Nanocrystals. *ACS Nano* 2013, 7, 2676–2685.
- (85) Walavalkar, S. S.; Hofmann, C. E.; Homyk, A. P.; Henry, M. D.; Atwater, H. A.; Scherer, A. Tunable Visible and Near-IR Emission from Sub-10 Nm Etched Single-Crystal Si Nanopillars. *Nano Lett.* **2010**, *10*, 4423–4428.
- (86) Dasog, M.; de los Reyes, G. B.; Titova, L. v.; Hegmann, F. A.; Veinot, J. G. C. Size vs Surface: Tuning the Photoluminescence of Freestanding Silicon Nanocrystals Across the Visible Spectrum via Surface Groups. ACS Nano 2014, 8, 9636–9648.
- (87) Shen, H.; Yu, Z.; Wang, J.; Lu, M.; Qiao, C.; Su, W.-S.; Zheng, Y.; Zhang, R.; Jia, Y.; Chen, L.; Wang, C.; Ho, K.; Wang, S.

Luminescence Mechanism in Hydrogenated Silicon Quantum Dots with a Single Oxygen Ligand. *Nanoscale Adv.* **2021**, *3*, 2245–2251. (88) Holmes, J. D.; Johnston, K. P.; Doty, R. C.; Korgel, B. A. Control of Thickness and Orientation of Solution-Grown Silicon Nanowires. *Science* **2000**, *287*, 1471–1473.